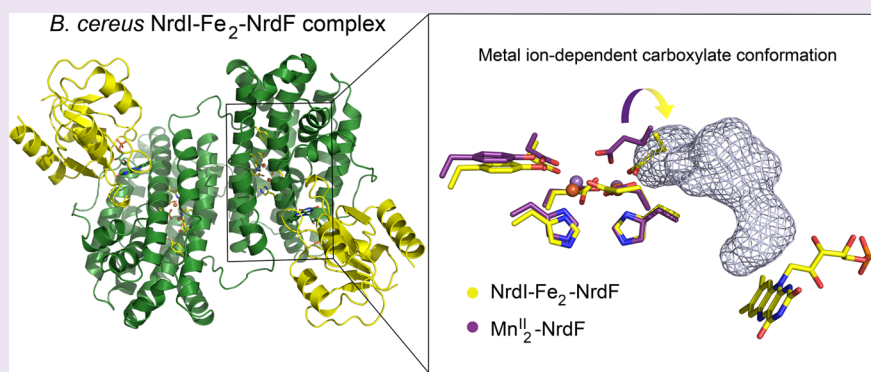


# Crystal Structure of *Bacillus cereus* Class Ib Ribonucleotide Reductase Di-iron NrdF in Complex with NrdI

Marta Hammerstad, Hans-Petter Hersleth,\* Ane B. Tomter, Åsmund K. Røhr, and K. Kristoffer Andersson

Department of Biosciences, University of Oslo, P.O. Box 1066, Blindern, NO-0316 Oslo, Norway

 Supporting Information



**ABSTRACT:** Class Ib ribonucleotide reductases (RNRs) use a dimetal-tyrosyl radical ( $\text{Y}\bullet$ ) cofactor in their NrdF ( $\beta_2$ ) subunit to initiate ribonucleotide reduction in the NrdE ( $\alpha_2$ ) subunit. Contrary to the diferric tyrosyl radical ( $\text{Fe}^{\text{III}}_2\text{-Y}\bullet$ ) cofactor, which can self-assemble from  $\text{Fe}^{\text{II}}_2\text{-NrdF}$  and  $\text{O}_2$ , generation of the  $\text{Mn}^{\text{III}}_2\text{-Y}\bullet$  cofactor requires the reduced form of a flavoprotein, NrdI<sub>hq</sub>, and  $\text{O}_2$  for its assembly. Here we report the 1.8 Å resolution crystal structure of *Bacillus cereus*  $\text{Fe}_2\text{-NrdF}$  in complex with NrdI. Compared to the previously solved *Escherichia coli* NrdI- $\text{Mn}^{\text{II}}_2\text{-NrdF}$  structure, NrdI and NrdF binds similarly in *Bacillus cereus* through conserved core interactions. This protein–protein association seems to be unaffected by metal ion type bound in the NrdF subunit. The *Bacillus cereus*  $\text{Mn}^{\text{II}}_2\text{-NrdF}$  and  $\text{Fe}_2\text{-NrdF}$  structures, also presented here, show conformational flexibility of residues surrounding the NrdF metal ion site. The movement of one of the metal-coordinating carboxylates is linked to the metal type present at the dimetal site and not associated with NrdI-NrdF binding. This carboxylate conformation seems to be vital for the water network connecting the NrdF dimetal site and the flavin in NrdI. From these observations, we suggest that metal-dependent variations in carboxylate coordination geometries are important for active  $\text{Y}\bullet$  cofactor generation in class Ib RNRs. Additionally, we show that binding of NrdI to NrdF would structurally interfere with the suggested  $\alpha_2\beta_2$  (NrdE-NrdF) holoenzyme formation, suggesting the potential requirement for NrdI dissociation before NrdE-NrdF assembly after NrdI activation. The mode of interactions between the proteins involved in the class Ib RNR system is, however, not fully resolved.

Ribonucleotide reductases (RNRs) catalyze the conversion of ribonucleotides to their corresponding deoxyribonucleotides in all living organisms, providing the essential building blocks required for DNA replication and repair.<sup>1,2</sup> Class I RNRs consist of two homodimeric subunits:  $\alpha_2$  and  $\beta_2$ . Nucleotide reduction is initiated through the reversible one-electron oxidation of a conserved cysteine residue to a thiol radical in the  $\alpha_2$  subunits, initiated by a dinuclear metallocofactor and tyrosyl radical positioned in the  $\beta_2$  subunits.<sup>3</sup> Three subclasses of the class I enzymes have been characterized based on their metal ion composition and sequence: Ia, Ib, and Ic.<sup>4</sup> The class Ia RNRs are found in eukaryotes, some viruses, and some prokaryotes such as *Escherichia coli* (*Ec*) (the latter also containing the class Ib RNR), supplying deoxyribonucleotides during normal aerobic growth.<sup>3,5</sup> Enzyme activity requires a  $\mu$ -oxo-bridged diferric tyrosyl radical ( $\text{Fe}^{\text{III}}_2\text{-Y}\bullet$ ) cofactor localized in the  $\beta_2$  subunit (NrdB/R2).<sup>6</sup> The cofactor can be formed by self-assembly from apo-NrdB in the presence of  $\text{Fe}^{\text{II}}$  and  $\text{O}_2$ , forming the  $\text{Y}\bullet$  required for dNDP formation in the  $\alpha_2$  subunits

(NrdA/R1).<sup>7</sup> The class Ic RNR has so far been well characterized only in the obligate intracellular pathogen *Chlamydia trochomatis*. Subsequent studies have shown that its  $\beta_2$  subunit utilizes a stable, heterodinuclear  $\text{Mn}^{\text{IV}}\text{Fe}^{\text{III}}$  cofactor to initiate catalysis.<sup>8–11</sup> Class Ib RNRs are the primary sources of dNTPs for a wide variety of prokaryotes, such as *Mycobacterium tuberculosis* (*Mt*), *Corynebacterium ammoniagenes* (*Ca*), *Bacillus anthracis* (*Ba*), *Bacillus subtilis* (*), and *Bacillus cereus* (*Bc*).<sup>12</sup> The class Ib enzymes consist of the  $\alpha_2$  (NrdE/R1E) and  $\beta_2$  (NrdF/R2F) subunits,<sup>13</sup> where the active form in both class Ia and class Ib is believed to comprise an  $\alpha_2\beta_2$  stoichiometry.<sup>14,15</sup> The metallocofactor required for activity in class Ib RNRs has for several decades been known to consist of an  $\text{Fe}^{\text{III}}_2\text{-Y}\bullet$  cofactor, assembled *in vitro* similarly to the class Ia*

**Received:** June 17, 2013

**Accepted:** December 2, 2013

**Published:** December 2, 2013



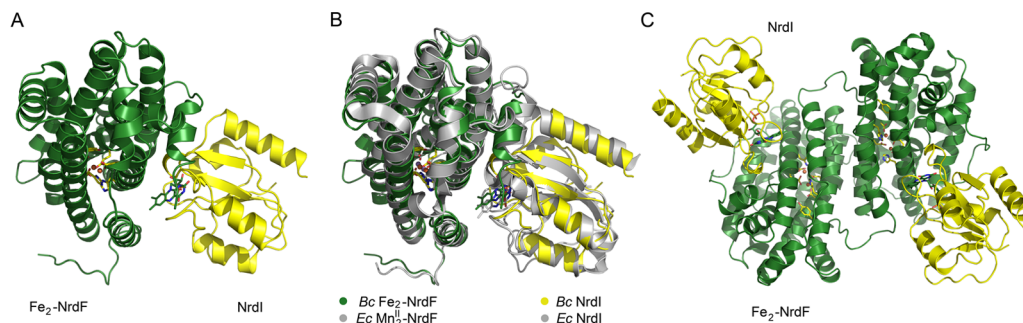


**Figure 1.** Structure of the NrdI-NrdF complex. (A) The overall structure of the *Bc* NrdI-Fe<sub>2</sub>-NrdF complex and (B) alignment of the *Bc* and *Ec* (PDB id: 3N39) NrdI-Fe<sub>2</sub>-NrdF and NrdI-Mn<sup>II</sup><sub>2</sub>-NrdF complexes, respectively. (C) The dimeric *Bc* NrdI-Fe<sub>2</sub>-NrdF complex, represented by the monomeric *Bc* NrdI-Fe<sub>2</sub>-NrdF (asymmetric unit) shown with its symmetry equivalent molecule. The FMN cofactor in NrdI and the residues in the active site of NrdF are represented as sticks and colored by atom type in *Bc* and colored gray in *Ec*. Fe ions are shown as orange spheres (*Bc*), and Mn<sup>II</sup> ions are shown as purple spheres (*Ec*).

enzymes.<sup>16,17</sup> However, recent studies have shown that the class Ib NrdF can also utilize an active Mn<sup>III</sup><sub>2</sub>-Y• cofactor for nucleotide reduction.<sup>18–20</sup> The Mn<sup>III</sup><sub>2</sub>-Y• cofactor can only be generated from the dimanganese(II) site (Mn<sup>II</sup><sub>2</sub>) in a self-assembly process in the presence of O<sub>2</sub> and the flavodoxin-like protein NrdI.<sup>18</sup> NrdI is found in all organisms with genomes coding for the class Ib RNR<sup>21</sup> and contains a flavin mononucleotide cofactor (FMN), demonstrated to be able to act as a two-electron reductant.<sup>22,23</sup> It has been proposed that NrdI, in its fully reduced hydroquinone form (NrdI<sub>hq</sub>, containing FMNH<sup>−</sup>), reacts with O<sub>2</sub> providing the oxidant, H<sub>2</sub>O<sub>2</sub> or O<sub>2</sub>•<sup>−</sup>, required for generation of the active Mn<sup>III</sup><sub>2</sub>-Y• cofactor.<sup>24–26</sup> Studies have shown that the Mn<sup>III</sup><sub>2</sub>-Y• cofactor can be formed both *in vitro* and *in vivo*,<sup>20,24</sup> and that the manganese form of the enzyme has a higher specific activity compared to the iron form, as in the case of *Ba*,<sup>27</sup> *Bc*,<sup>28</sup> and *Bs*,<sup>29</sup> all showing a 10-fold difference. It is still not understood how the *in vitro* process of cofactor assembly using identical metal coordinating ligands, but different metals and oxidants,<sup>30</sup> is controlled *in vivo*. Structural studies of *Ec* NrdF both in the Fe<sup>III</sup><sub>2</sub> and Mn<sup>III</sup><sub>2</sub> forms, as well as of the crystal structure of the Mn<sup>II</sup><sub>2</sub>-NrdF in complex with NrdI, give insight into Y• generation in NrdF.<sup>25</sup> The metal-binding residues are identical in most class Ia and Ib RNRs, where the dimetal clusters are coordinated by four carboxylates and two histidines.<sup>31</sup> The coordination environment in structures of *Ec* Mn<sup>II</sup><sub>2</sub>-NrdF and NrdI-NrdF complexes revealed an unusual structural feature involving Glu158 (*Ec* numbering), showing bridging of both metals in a μ-1,3 fashion.<sup>25</sup> This carboxylate conformation observed in the *Ec* structures is different from other reported RNR class I structures, where the corresponding Glu coordinates to metal site 2 alone. In these structures, Glu occupies the site of a Mn2 water ligand thought to be part of an ordered water network facilitating transport of the reactive oxidant from the NrdI flavin cofactor to the NrdF metal site, required for the generation of the Mn<sup>III</sup><sub>2</sub>-Y• cofactor.<sup>18</sup>

Here, we present the first crystal structure of the *Bc* class Ib NrdF in complex with the flavoprotein NrdI. In this 1.8 Å resolution crystal structure, the *Bc* NrdF is in the Fe<sub>2</sub> form, and the Glu161 (*Bc* numbering) coordinates to only metal site 2, as seen for most class Ib NrdF structures. This is in contrast to what was observed in the *Ec* Mn<sup>II</sup><sub>2</sub>-NrdF and NrdI-Mn<sup>II</sup><sub>2</sub>-NrdF structures, where Glu bridges both metals in a μ-1,3 fashion opening up for an ordered water network to the FMN site. In both the *Bc* NrdI-Fe<sub>2</sub>-NrdF and Fe<sub>2</sub>-NrdF structures, this water network and channel is blocked by the bidentate coordination

of Glu161 only to the Fe2 site. However, in the *Bc* Mn<sup>II</sup><sub>2</sub>-NrdF crystal structure, also presented here, Glu161 shows variations in this carboxylate conformation, with one conformation bridging both metals in a μ-1,3 fashion, revealing the water network. The carboxylate variations in the different NrdI-NrdF complexes, as well as NrdF structures, indicate that flexibility in coordinating amino acids is possible, almost in a gating fashion, and is likely important for metal cofactor and tyrosyl radical generation.

## RESULTS AND DISCUSSION

In this work, we present six crystal structures of the *Bc* class Ib RNR small subunit NrdF, including two structures of NrdF in complex with NrdI (NrdI-NrdF-1 and -2), Fe<sub>2</sub>-NrdF, Mn<sup>II</sup><sub>2</sub>-NrdF, and two structures of apo-NrdF (apo-NrdF-1 and -2).

**Overall Structure of the *Bc* Fe<sub>2</sub>-NrdF, Mn<sub>2</sub>-NrdF, and NrdI-NrdF Complex.** Both the 2.1 Å (NrdI-NrdF-1) and 1.8 Å (NrdI-NrdF-2) resolution crystal structures of *Bc* NrdI-NrdF were obtained by co-crystallizing NrdF with an equimolar amount of NrdI. The asymmetric unit contains one monomer of NrdI in complex with one monomer of NrdF, in which the overall architecture strongly resembles the *Ec* NrdI-NrdF structure reported earlier by Boal et al.<sup>25</sup> The overall structure of the 2.1 Å resolution *Bc* NrdI-NrdF protein complex is shown in Figure 1A and C, while a structural alignment of the *Bc* and *Ec* NrdI-NrdF complexes is shown in Figure 1B and Supplementary Figure S1. Structural similarity between the *Bc* and *Ec* monomeric NrdI-NrdF complexes has been calculated to an RMSD value of 1.42 Å, while structural similarity between the dimeric NrdI-NrdF structures have an RMSD of 1.78 Å. The RMSDs for the *Bc* and *Ec* NrdF and NrdI structures individually (from the crystal complexes) are 1.23 and 1.05 Å, respectively. This shows that the NrdF and NrdI bind similarly to each other in *Ec* and *Bc*, but with some small structural variations (see below). The final model for NrdI-NrdF-1 consists of residues 1–290 out of 322 in NrdF and residues 1–117 out of 119 in NrdI and are refined to final *R*<sub>work</sub>/*R*<sub>free</sub> values of 17.7%/23.3%. The NrdI-NrdF-2 structure consists of residues 1–290 in NrdF and 1–118 in NrdI and are refined to final *R*<sub>work</sub>/*R*<sub>free</sub> values of 16.7%/20.9%. Both the NrdI-NrdF and the different NrdF structures show well-defined electron density for the modeled residues. The 2.1 and 1.9 Å resolution crystal structures of *Bc* Fe<sub>2</sub>-NrdF and Mn<sup>II</sup><sub>2</sub>-NrdF, respectively, contain two molecules in the asymmetric unit, with the final models consisting of residues 1–287 out of 322 in monomers A

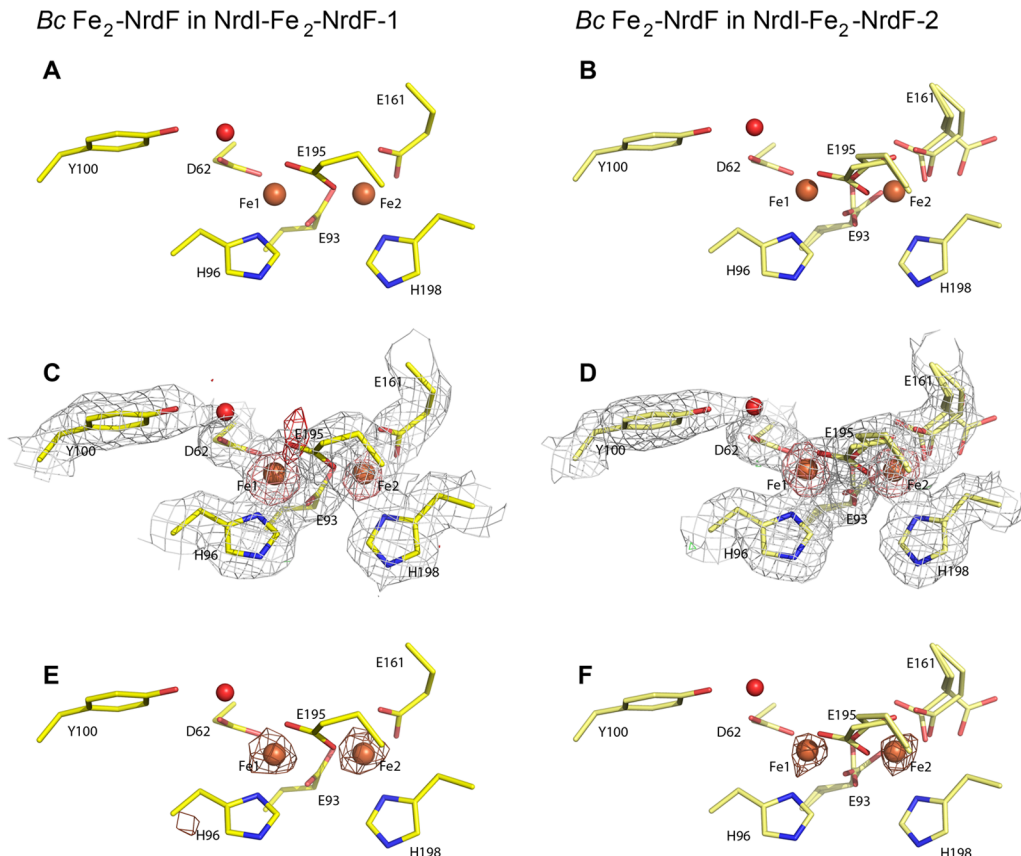


**Figure 2.** Metal ion sites in the two *Bc* NrdI-Fe<sub>2</sub>-NrdF complex structures. (A, C, and E) The metal site in NrdI-Fe<sub>2</sub>-NrdF-1 and (B, D, and F) the metal site in NrdI-Fe<sub>2</sub>-NrdF-2. The Fe ions are shown as orange spheres, and the coordinating amino acids and Tyr100 are represented as sticks and colored by atom type. In panels C and D, the  $2F_o - F_c$  electron density map (gray) is contoured at  $1\sigma$ , while the  $F_o - F_c$  map is shown as green mesh ( $3\sigma$ ) and red mesh ( $-3\sigma$ ). The omit map surrounding the Fe ions is contoured at  $6\sigma$  (salmon). The Fe ions are modeled with 90% (C) and 50% (D) occupancy. For panels E and F, anomalous maps are included, contoured at  $3.5\sigma$  (brown).

and B for both structures. The structures are refined to final  $R_{\text{work}}/R_{\text{free}}$  values of 18.5%/23.5% and 21.0%/26.0%, respectively. The two *Bc* apo-NrdF structures belong to different crystal forms. Apo-NrdF-2 (2.0 Å) belongs to space group  $P2_1$  as the *Bc* Fe/Mn-NrdF structures and contains residues 1–287/1–288 for the two monomers with final  $R_{\text{work}}/R_{\text{free}}$  values of 20.8%/26.0%. Apo-NrdF-1 (2.2 Å) belongs to space group  $C2$ , also consisting of two monomers, and was refined to final  $R_{\text{work}}/R_{\text{free}}$  values of 17.6%/24.3%. The overall structure of *Bc* NrdF in the different NrdI-NrdF and NrdF structures presented here are very similar (Supplementary Figure S2A). However, residues 26–31 in NrdI-NrdF-1 and monomer B of apo-NrdF-1 have a more helical conformation compared to the other structures (Supplementary Figure S2C and D). Due to a different crystal packing, 13 more residues of the flexible C-terminal end were built into the electron density of monomer A of apo-NrdF-1 (Supplementary Figure S2B), with the two resulting monomers containing residues 1–300/1–287, respectively. These additionally built in residues point into the area where interaction with NrdE is suggested,<sup>14</sup> indicating that the flexible C-terminal could become ordered through interaction with NrdE.

**Structure and Coordination Environment of the Crystal Complex Metal Cluster Site.** The overall structure of the metal cluster coordination site in the *Bc* NrdI-NrdF structure strongly resembles other class Ib NrdF structures,<sup>13,19,30,32,33</sup> except for the *Ec* Mn<sup>II</sup><sub>2</sub>-NrdFs<sup>25</sup> and the *Bc*

Mn<sup>II</sup><sub>2</sub>-NrdF presented in this paper. Both *Bc* NrdI-NrdF complex structures have been obtained with iron in the NrdF dimetal sites (Figure 2). For the NrdI-Fe<sub>2</sub>-NrdF-1 structure modeled with 90% iron occupancy, the Fe sites are four- and five-coordinated, respectively, with an Fe–Fe distance of 3.9 Å, Glu195 in a  $\mu$ -1,3 coordination, and Glu161 bidentate to Fe2 (Figure 2A, C, and E). The coordination and the long Fe–Fe distance is consistent with previously reported ferrous (Fe<sup>II</sup>) iron NrdF/B structures.<sup>13,19,30,32,33</sup> The Fe omit map shown in Figure 2C and D and the anomalous difference map at 1.0 Å wavelength confirm the presence of metals in the di-Fe sites (Figure 2E and F). In the 1.8 Å NrdI-Fe<sub>2</sub>-NrdF-2 structure, similar coordination and Fe–Fe distance is observed; however, additional alternative conformations are modeled for Glu195, Glu93, and Glu161 (Figure 2B, D, and F). This could partly be due to the lower iron occupancy in the di-Fe sites (50%). The X-ray doses absorbed by the different crystals in this study (Table 1) are within the recommended Henderson limit of 20 MGy to avoid considerable radiation damage of protein crystals.<sup>34</sup> Nevertheless, X-ray induced radiation damage of metal sites occurs on a much shorter time scale.<sup>35</sup> Studies on RNR have shown a fast reduction of the oxidized metal ion states;<sup>36,37</sup> however, the structures presented here are considered to already be in the reduced states, and therefore X-ray induced changes are limited.

***Bc* Fe<sub>2</sub>-NrdF Coordination Environment.** The crystal structure of the dimeric *Bc* Fe<sub>2</sub>-NrdF has been modeled with

**Table 1.** Data Collection and Refinement Statistics

	<i>Bc Mn<sup>II</sup><sub>2</sub>-NrdF</i>	<i>Bc Fe<sub>2</sub>-NrdF</i>	<i>Bc NrdI-NrdF-1</i>	<i>Bc NrdI-NrdF-2</i>
Crystal Data				
space group	<i>P</i> 2 <sub>1</sub>	<i>P</i> 2 <sub>1</sub>	<i>C</i> 222 <sub>1</sub>	<i>C</i> 222 <sub>1</sub>
<i>a</i> , <i>b</i> , <i>c</i> (Å)	61.9/49.2/98.5	62.0/49.3/98.5	59.3/125.0/142.6	59.5/124.7/141.3
$\alpha$ , $\beta$ , $\gamma$ (deg)	90.0/107.2/90.0	90.0/107.2/90.0	90.0/90.0/90.0	90.0/90.0/90.0
crystal size (μm <sup>3</sup> )	40 × 100 × 200	40 × 100 × 200	75 × 75 × 200	100 × 100 × 200
Data Collection				
X-ray source	ESRF-ID29	ESRF-ID29	ESRF-ID29	SLS-PXII-X10SA
wavelength (Å)	0.9724	0.9724	0.9763	0.9999
flux (photons/s)	1660 × 10 <sup>9</sup>	1600 × 10 <sup>9</sup>	75 × 10 <sup>9</sup>	225 × 10 <sup>9</sup>
beam size (μm <sup>2</sup> )	30 × 50	30 × 50	30 × 50	100 × 100
total exposure (s)	19	30	150	120
absorbed X-ray dose (MGy)	7.4	11.3	2.4	1.0
resolution range (Å)	47.0–1.9/2.0–1.9	47.0–2.1/2.2–2.1	62.5–2.1/2.2–2.1	53.7–1.8/1.9–1.8
temperature (K)	100	100	100	100
completeness (%) <sup>a</sup>	90.4/92.9	88.7/84.9	98.5/98.9	98.2/99.3
redundancy <sup>a</sup>	2.1/2.1	2.8/2.7	3.9/3.9	4.1/4.1
<i>I</i> / $\sigma$ ( <i>I</i> ) <sup>a</sup>	11.3/2.1	5.7/2.7	8.6/2.8	11.3/2.9
<i>R</i> <sub>sym</sub> <sup>a,b</sup>	10.7/37.9	10.1/30.1	9.5/43.7	5.9/45.0
Refinement Statistics				
<i>R</i> <sub>work</sub> (%) <sup>c</sup>	18.4	21.0	17.7	16.7
<i>R</i> <sub>free</sub> (%) <sup>d</sup>	23.4	26.0	23.3	20.9
Model Content				
amino acids	574	574	407	408
Fe ions (occupancy)	-	4 (100%)	2 (90%)	2 (50%)
Mn ions (occupancy)	4(100,90,100,100%)	-	-	-
Cl <sup>-</sup> ions	-	-	1	5
water molecules	166	61	117	196
FMN cofactors	-	-	1	1
molecules per asu	2	2	1 + 1	1 + 1
solvent content (%)	40.1	42.7	54.2	50.8
unmodelled residues	288–322 (both monomers)	288–322 (both monomers)	291–322 (NrdF), 117–119 (NrdI)	291–322 (NrdF), 118–119 (NrdI)
volume not occupied by model (%)	28.8	30.7	45.2	43.0
Model Analysis				
mean overall isotropic B-factor (Å <sup>2</sup> )	19.8	19.5	32.9	32.1
Ramachandran plot: ratio in most favored/other allowed regions/generously allowed regions (%)	96.9/3.1/-	96.9/3.1/-	92.7/6.5/0.8	95.9/3.5/0.5
estimated overall coordinate error based on <i>R</i> <sub>work</sub> /maximum likelihood (Å)	0.19/0.11	0.33/0.15	0.18/0.12	0.11/0.084
RMSD bonds (Å)/angles (deg)	0.019/1.90	0.017/1.78	0.019/2.04	0.020/1.90
PDB code	4BMU	4BMT	4BMP	4BMO

<sup>a</sup>The value before the slash is for all data, and the value after the slash is for the data in the highest resolution shell. <sup>b</sup>*R*<sub>sym</sub> =  $\Sigma |I - \langle I \rangle| / \Sigma I$ . <sup>c</sup>*R*<sub>work</sub> =  $\Sigma (|F_o| - |F_c|) / \Sigma |F_o|$ . <sup>d</sup>*R*<sub>free</sub> is the *R*<sub>work</sub> calculated on the 5% reflections excluded for refinement.

full metal occupancy at the dimetal sites. The higher B-factor of the Fe1 sites in Fe<sub>2</sub>-NrdF could indicate lower occupancy. The di-Fe sites in the ferrous soaked NrdF structure have higher coordination compared to the NrdI-Fe<sub>2</sub>-NrdF structures (Figures 2, 3, and 4A). For monomer A, contrary to NrdI-Fe<sub>2</sub>-NrdF-1, Glu195 has moved to a  $\mu$ -( $\eta^1$ - $\eta^2$ ) coordination opening up for a water coordinating to Fe1 instead of a water molecule hydrogen-bound to Tyr100, the residue responsible for tyrosyl radical (Y•) generation in *Bc*. This results in the Fe sites becoming five- and six-coordinated, respectively, differing from what has been observed by circular dichroism and magnetic circular dichroism on RNR protein solutions.<sup>2,38</sup> The  $\mu$ -( $\eta^1$ - $\eta^2$ ) coordination of Glu195 (*Bc* numbering) in *Bc* Fe<sub>2</sub>-NrdF is also observed in *Ec* Fe<sup>II</sup><sub>2</sub>-NrdB (without the water coordinating to Fe1) and in *Ec* Mn<sup>II</sup><sub>2</sub>-NrdF structures, while the Fe<sup>II</sup><sub>2</sub>-NrdF structures from *Ca*, *Salmonella typhimurium* (*St*),

*Mt*, and the Mn<sup>II</sup><sub>2</sub>-NrdF structures from *Ca*, *Ec*, and *Bs* all show the  $\mu$ -1,3 coordination (Figure 4B).<sup>13,25,30,32,33</sup> In monomer B of *Bc* Fe<sub>2</sub>-NrdF, Glu161 coordinates to Fe2 in a monodentate way instead of bidentate, resulting in both di-Fe sites being five coordinated (Figure 3A–D).

***Bc Mn<sup>II</sup><sub>2</sub>-NrdF Coordination Environment and Glu161 Movement.*** The *Bc Mn<sup>II</sup><sub>2</sub>-NrdF* structure has been modeled with full occupancy at the dimetal sites (except for Mn2 in monomer A with 90% occupancy) (Figure 3E–H) and shows higher coordination for the dimetal site than in the *Bc Fe<sub>2</sub>-NrdF* with both Mn-sites being six-coordinated similar to what is observed in *Ec*. In the *Bc Mn<sup>II</sup><sub>2</sub>-NrdF* structure, Glu161 shows great flexibility. Two and three alternative conformations have been modeled at the Glu161 site in monomers A and B, respectively. In monomer A, one coordinates to metal site 2 alone, in a bidentate fashion (33%) as seen in the *Bc Fe<sub>2</sub>-NrdF*

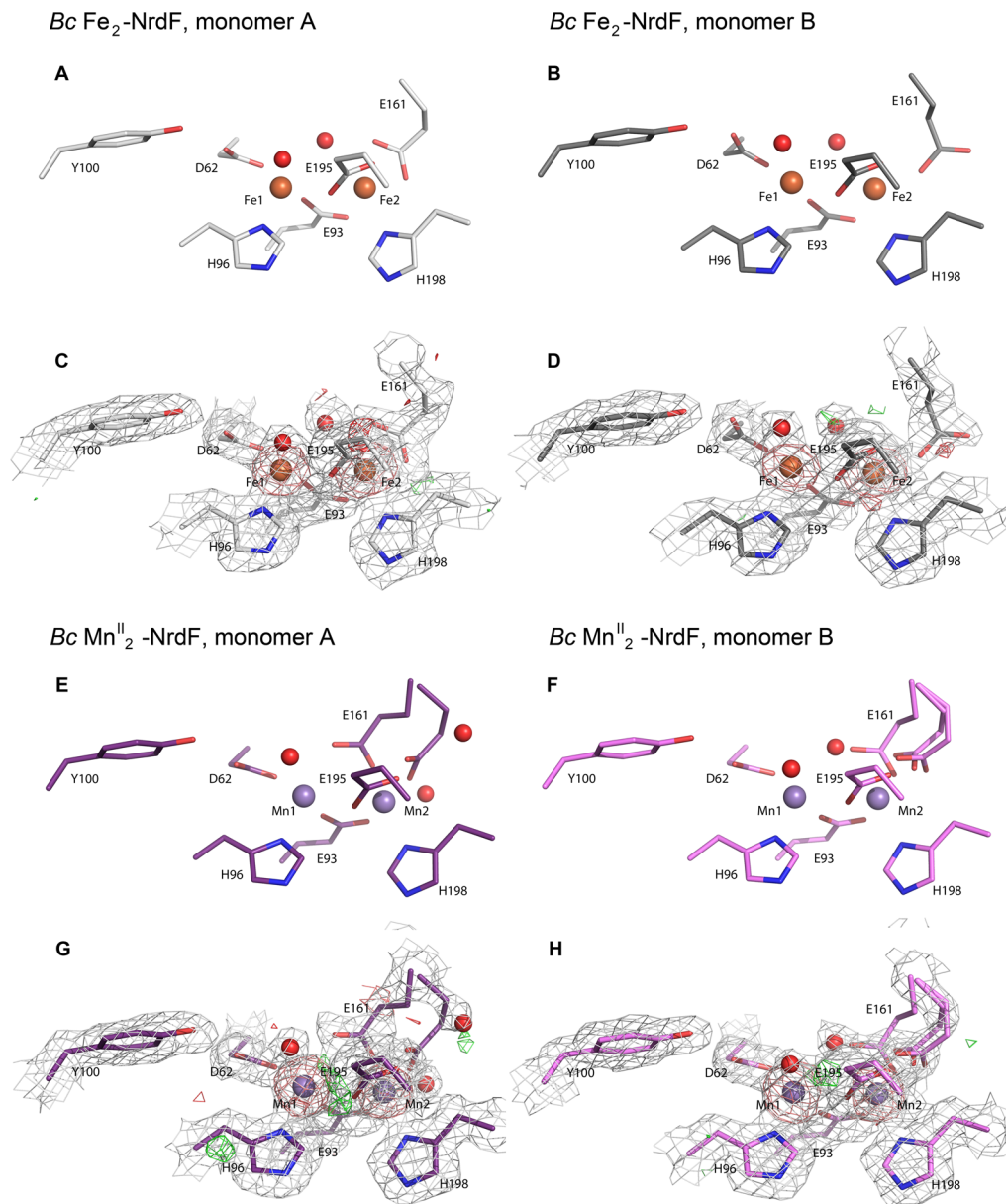


**Figure 3.** Metal ion sites in *Bc*  $\text{Fe}_2\text{-NrdF}$  and  $\text{Mn}^{\text{II}}_2\text{-NrdF}$ . (A and C) Monomer A in *Bc*  $\text{Fe}_2\text{-NrdF}$ , (B and D) monomer B in *Bc*  $\text{Fe}_2\text{-NrdF}$ . (E and G) Monomer A in *Bc*  $\text{Mn}^{\text{II}}_2\text{-NrdF}$  and (F and H) monomer B in *Bc*  $\text{Mn}^{\text{II}}_2\text{-NrdF}$ . The Fe ions are shown as orange spheres, Mn ions as purple spheres, and the coordinating amino acids and Tyr100 are represented as sticks and colored by atom type. The  $2F_o - F_c$  electron density map (gray) is contoured at  $1\sigma$  and the  $F_o - F_c$  map is shown as green mesh ( $3\sigma$ ) and red mesh ( $-3\sigma$ ), whereas the omit map (salmon) surrounding the Fe or Mn ions is contoured at  $6\sigma$  (C, D, G and H). Glu161 coordinates to Fe2 in a bidentate fashion in monomer A and in a monodentate fashion in monomer B of  $\text{Fe}_2\text{-NrdF}$  (A–D). In  $\text{Mn}^{\text{II}}_2\text{-NrdF}$ , two and three different conformations are observed for Glu161 in monomers A and B, respectively, varying between a bidentate mode coordinating to Mn2 alone and a conformation bridging both metals (E–H).

structures, while the other major conformations (67%) bridge both metals similar to the  $\mu\text{-}1,3$  coordination observed in the *Ec* NrdI- $\text{Mn}^{\text{II}}_2\text{-NrdF}$  and  $\text{Mn}^{\text{II}}_2\text{-NrdF}$  structures (Figure 4B). This opens up for a water coordinating to the Mn2 site and an extended water network (as discussed below). The  $\mu\text{-}1,3$  coordination of this Glu residue was not reported for the *Bs*  $\text{Mn}^{\text{II}}_2\text{-NrdF}$  structure (PDB id: 4DR0)<sup>33</sup> and thereby not supporting a direct Fe to Mn induced movement of Glu158 (*Ec* numbering) as observed in *Ec* and now in *Bc*. However, although Glu164 (*Bs* numbering) is reported to coordinate only to Mn2 in a bidentate fashion, some negative density can be seen in the difference map at the modeled Glu164, and some positive density where an alternative conformation for Glu164

bridging both metals in a  $\mu\text{-}1,3$  fashion would be positioned, supporting flexibility at the Glu161 (*Bc* numbering) site. In the *Ec* structures, the main-chain between Phe162 and Glu158 (*Ec* numbering) has an altered conformation between the Fe and Mn structures, while in the *Bc* structures, the main-chain between Phe165 and Glu161 (*Bc* numbering) is more similar, resulting in an incomplete  $\mu\text{-}1,3$  coordination of Glu161 in *Bc*  $\text{Mn}^{\text{II}}_2\text{-NrdF}$  (Supplementary Figure S3). The observed difference could be due to the fact that the *Ec* structures are co-crystallized with  $\text{Mn}^{\text{II}}$ , while the *Bc* crystals have been soaked with  $\text{Mn}^{\text{II}}$ , thereby allowing less structural adjustments in *Bc*. This further indicates that the Glu161 movement is linked to the Mn substitution. The movement of Glu161 in *Bc* from a

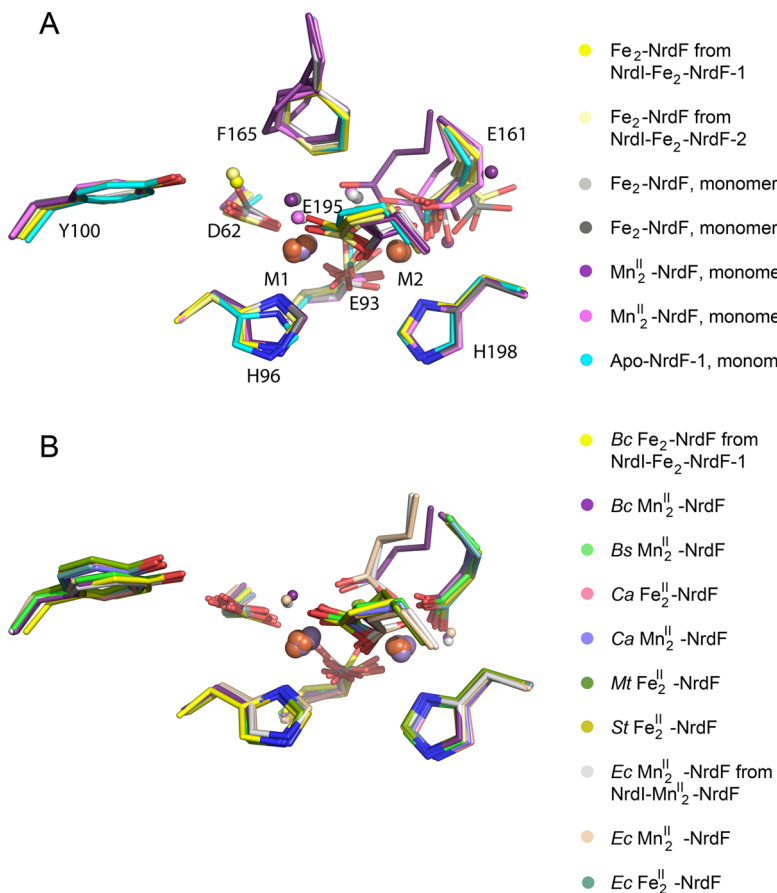


**Figure 4.** Overlay of metal sites in different NrdF crystal structures. (A) Metal sites in the different *Bc* NrdF crystal structures. (B) Metal sites in class Ib  $\beta_2$  structures from different organisms. The Mn ions and Fe ions are colored as purple and orange spheres, respectively, and the coordinating amino acids, as well as Tyr100 and Phe165, are represented as sticks and colored by atom type. Structures compared in panel B (A chains) are; *Bc* NrdI-Fe<sub>2</sub>-NrdF-1, *Ec* NrdI-Mn<sup>II</sup>-NrdF complex (PDB id: 3N39),<sup>25</sup> *Bc* Mn<sup>II</sup>-NrdF, *Ec* Mn<sup>II</sup>-NrdF (PDB id: 3N37),<sup>25</sup> *Ec* Fe<sup>II</sup>-NrdF (PDB id: 3N38),<sup>25</sup> *Bs* Mn<sup>II</sup>-NrdF (PDB id: 4DR0),<sup>33</sup> *Ca* Mn<sup>II</sup>-NrdF (PDB id: 1KGP),<sup>30</sup> *Ca* Fe<sup>II</sup>-NrdF (PDB id: 1KGO),<sup>30</sup> *Mt* Fe<sup>II</sup>-NrdF (PDB id: 1UZR),<sup>32</sup> and *St* Fe<sup>II</sup>-NrdF (PDB id: 1R2F).<sup>13</sup>

bidentate coordination of metal site 2 to a  $\mu$ -1,3 coordination is further associated with a rotation of Phe165 (Figure 4A and Supplementary Figure S3), which is also observed in *Ec* between the Fe<sub>2</sub>-NrdF and Mn<sup>II</sup>-NrdF/NrdI-Mn<sup>II</sup>-NrdF structures.<sup>25</sup> Moreover, if the flexibility of Glu161 in the *Bc* Mn<sup>II</sup>-NrdF structures is influenced by a minor iron contamination, as previously reported in work by Tomter et al.,<sup>38</sup> an inhomogeneous metalation in metal site 2 would even stronger support a metal-type-dependent movement of Glu161. The redox state and the pH of the metal ion cluster is also known to influence the conformation of the coordinating residues.<sup>6,39</sup> The metal cluster environments in the two *Bc* apo-NrdF structures are shown in Supplementary Figures S4 and S5. The trends for Glu195 and Glu93 coordination seem more unclear, while Glu161 coordination appears to give important insight into the distinction between the Fe- and Mn-NrdF/NrdI-NrdF structures (Figure 4A and B). In both *Bc* NrdI-Fe<sub>2</sub>-NrdF complex crystals, Glu161 coordinates bidentate to iron site 2 alone, opposite to what is seen in the *Ec* NrdI-Mn<sup>II</sup>-NrdF structure, where the corresponding carboxylate ligand bridges both metals in a  $\mu$ -1,3 fashion (Figure 4B). It has been proposed that the latter conformation allows greater access of a manganese-bound water ligand, hydrogen-bonded to an ordered water network facilitating oxidant transport from the NrdI FMN cofactor.<sup>25</sup> The  $\mu$ -1,3 coordination of Glu161 is

observed in both the *Ec* Mn<sup>II</sup>-NrdF structure and the *Bc* Mn<sup>II</sup>-NrdF structure (major conformation in monomer A), the latter presented here. The *Bc* Mn<sup>II</sup>-NrdF and *Bc* Fe<sub>2</sub>-NrdF structures presented here are therefore important toward a more generalized understanding of the metal-ion-dependent movement of this Glu residue with respect to NrdF activation. These observations support greater flexibility of the residues surrounding the class Ib NrdF metal sites and that variations in the carboxylate conformations seem to be linked to the metal-type present at the dimetal site, rather than induced by NrdI binding to NrdF, as also supported by NrdI-NrdF binding studies in *Ba* apo, Fe-, and Mn-NrdF.<sup>27</sup>

**NrdI-NrdF Interface Solvent Channel.** In the *Ec* and *Bc* NrdI-NrdF complexes, the proposed solvent-accessible channel extends from the vicinity of the metal site 2 in NrdF to the FMN cofactor of NrdI (Figure 5). This channel is structurally conserved in *Bc* and *Ec* NrdF with identical side-chain geometries of the lining residues Ser157/154, Tyr166/163, Ser162/159, Asn267/264, Lys263/260 and main-chain C=O for Glu195/192, Ser196/Ala193 (*Bc/Ec* numbering). In the interface between NrdF and NrdI, the water network is slightly altered, due to Tyr 197 in *Ec* replacing Val200 in *Bc*; however, FMN is also slightly shifted. Unlike observed in the *Ec* Mn<sup>II</sup>-NrdF structures with Glu158 in a  $\mu$ -1,3 coordination, the solvent channel modeled in the *Bc* NrdI-NrdF complex is

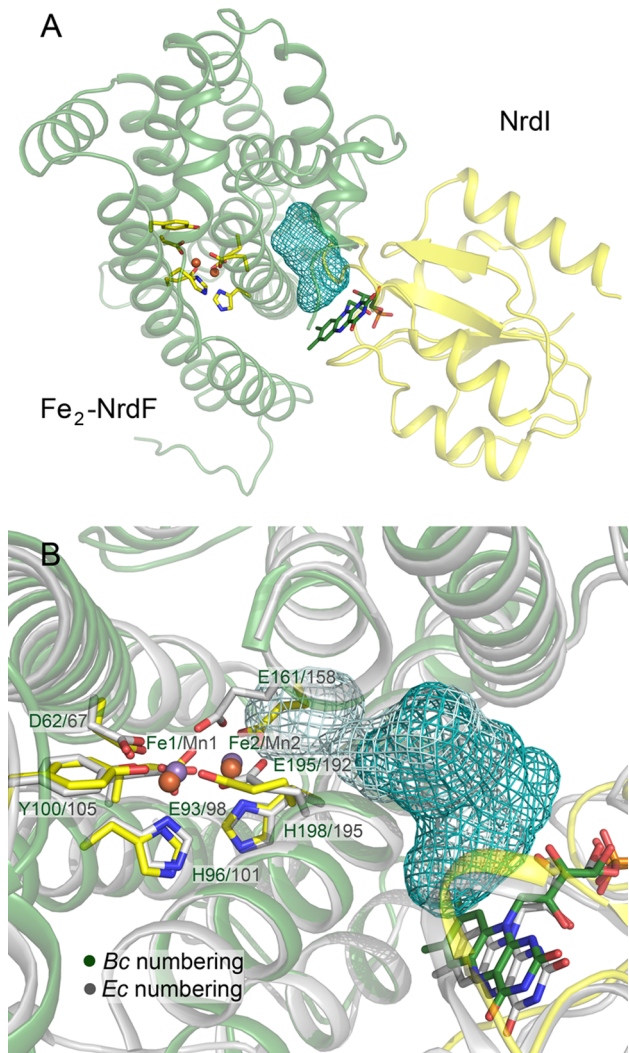


**Figure 5.** NrdI-NrdF solvent channel. (A) The *Bc* NrdI- $\text{Fe}_2$ -NrdF complex structures showing the hydrophilic channel connecting the active site in  $\text{Fe}_2$ -NrdF with the FMN cofactor in NrdI, calculated using a 1.4 Å probe radius, and (B) structural alignment of the *Bc* and *Ec* (PDB id: 3N39) NrdI- $\text{Fe}_2$ -NrdF and NrdI- $\text{Mn}^{\text{II}}_2$ -NrdF complexes, respectively, showing a closer view of the solvent channel (*Bc*; blue mesh, *Ec*; cyan mesh) connecting the NrdF and NrdI cofactors. *Bc* NrdI is shown as a yellow ribbon diagram and *Bc*  $\text{Fe}_2$ -NrdF as a green ribbon diagram, whereas the FMN cofactor in *Bc* NrdI and the residues in the active site of *Bc*  $\text{Fe}_2$ -NrdF are represented as sticks and colored by atom type. The *Ec* structure is shown in gray. Fe ions are shown as orange spheres (*Bc*), while  $\text{Mn}^{\text{II}}$  ions are shown as purple spheres (*Ec*). The Glu161 conformation in the *Bc* structure occupies the terminal part of the solvent channel, as modeled for the *Ec* structure, preventing the solvent channel in *Bc* from accessing the  $\text{Fe}_2$ -NrdF site.

prevented from accessing the  $\text{Fe}_2$ -NrdF site largely due to the bidentate coordination mode of Glu161 to Fe2, blocking the channel (Figure 5). Only in the case of the *Ec* NrdI- $\text{Mn}^{\text{II}}_2$ -NrdF structure does Glu158 allow full access of the solvent channel directly to the vicinity of the  $\text{Mn}^{\text{II}}_2$  site. A similar water network is also seen around the Mn2 site in the *Bc*  $\text{Mn}^{\text{II}}_2$ -NrdF structure (Figure 3E and G). The NrdI-NrdF channel modeled for the *Bc* complex, and compared to the *Ec* complex, is shown in Figure 5A and B, respectively. Different Glu161 conformations observed for the *Ec* NrdI- $\text{Mn}^{\text{II}}_2$ -NrdF and *Bc* NrdI- $\text{Fe}_2$ -NrdF complex structures indicate that variations in the NrdF active

site geometries might be present during active cofactor formation. The different geometries are likely not affected by NrdI binding to NrdF in protein complex formation. Highly similar NrdI-NrdF interfaces in both complexes are observed (see below), regardless of metal ion bound in the NrdF active site.

**NrdF Interface with NrdI.** The overall structure comparison of *Ec* and *Bc* NrdI-NrdF shows that the overall interaction between NrdF and NrdI is similar in the two organisms; however, the binding of NrdI to NrdF in *Bc* is slightly rotated compared to NrdI-NrdF binding in *Ec* (Supplementary Figure S1). The amino acids lining the *Bc* and *Ec* NrdI-NrdF interface show a high level of conservation. This is a general attribute for all class Ib RNRs, supported by the high sequence similarity<sup>33</sup> at the interface region, supporting invariable NrdI binding to the NrdF surface for class Ib RNRs. The charged and polar residues lining the NrdI-NrdF interface in both *Ec* and *Bc* complex structures create a hydrophilic environment consistent with channeling of a hydrophilic oxidant:  $\text{H}_2\text{O}_2$  or  $\text{O}_2\bullet^-$  for generation of the active  $\text{Mn}^{\text{III}}_2\text{-Y}\bullet$  cofactor in class Ib RNRs. One variation between the two complex structures of NrdI-NrdF in *Bc* and *Ec* is the distance between the NrdI flavin plane to the NrdF interface, which is 0.4 Å closer (based on whole structure alignment as measured from NS of FMN), for the *Bc* structure, creating a narrower interface (Figure 1B). A comparison of the *Bc* and *Ec* NrdI-NrdF structures, showing an ordered and identical hydrogen bonding network between conserved residues lining the core interface in both structures, is shown in Figure 6A and B. This core interface is likely essential for recognition between NrdFs and NrdIs in class Ib RNRs. Frequently, proteins involved solely in electron transfer do not interact in a well-defined orientation,<sup>40</sup> and therefore, the observation of a conserved binding-core between NrdI and NrdF supports that the complex is important for more than pure electron transfer, as it also generates a channel for the transfer of  $\text{H}_2\text{O}_2$  or  $\text{O}_2\bullet^-$ . Outside this core region, however, residues in the protein interface are not conserved, probably leading to a small rotation of NrdI relative to NrdF as observed between the *Bc* and *Ec* NrdI-NrdF structures (Supplementary Figure S1). While the core region governs recognition, amino acid differences outside the core must be important for the variations observed in NrdI-NrdF binding in *Ec* and the *Bacillus* species, where the association is much stronger in *Ec* than in *Bacillus*.<sup>18,22,27,28</sup> The conserved core interface region on the NrdF surface, as observed in the *Bc* and *Ec* NrdI-NrdF complex structures, is not present in the class Ia R2/NrdB, as shown in the structural alignment of the *Bc* NrdF and *Ec* NrdB structures<sup>41</sup> (Supplementary Figure S6). The structural differences in NrdBs, compared to NrdFs, do not support binding to NrdI, as observed in the class Ib NrdI-NrdF complex structures.<sup>25</sup> Moreover, the conserved class Ib NrdF interface region is also absent in eukaryotic class Ia R2 structures, as observed in mouse R2<sup>39</sup> and human p53R2.<sup>42</sup>

**Spectroscopic Similarity between NrdI and NrdI-NrdF.** Single-crystal light absorption measurements performed on crystals of *Bc* NrdI and *Bc* NrdI-NrdF show similar flavin spectra, indicating little or no influence on the NrdI FMN cofactor upon NrdF binding. Figure 6C shows the spectra obtained from the two crystals (*Bc* NrdI and *Bc* NrdI-NrdF) both containing NrdI in its oxidized ( $\text{NrdI}_{\text{ox}}$ ) form. The light absorption spectrum of a crystal depends on crystal orientation relative to the incident beam, causing small variations in the shapes of different peaks.<sup>43</sup> High structural similarity is

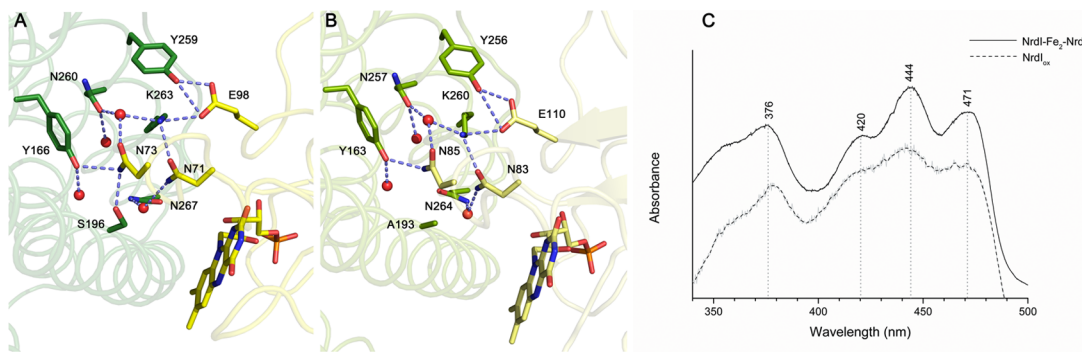


**Figure 6.** NrdI-NrdF protein–protein interface and single-crystal light absorption spectra. Comparison of the conserved hydrogen bonding network in the (A) *Bc* and (B) *Ec* (PDB id: 3N39) NrdI-NrdF crystal structures. NrdF residues are colored green, while NrdI residues are colored yellow. (C) Single-crystal light absorption spectra of *Bc* NrdI (dashed) and NrdI-NrdF (solid). Typical features of the oxidized state of the flavin cofactor are observed for the NrdI<sub>ox</sub> crystal and similar features are in the NrdI-NrdF crystal, regardless of the interaction with NrdF. A weaker signal is observed for the NrdI spectrum, largely due to crystal thickness.

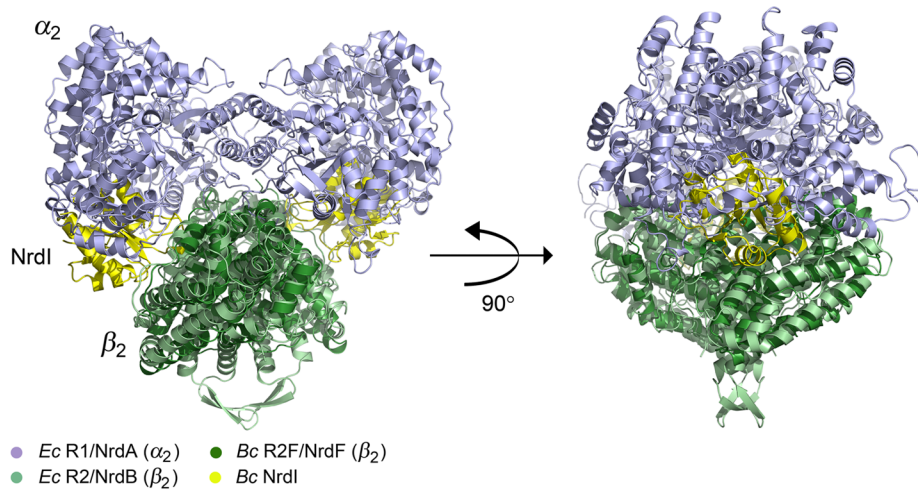


**Figure 7.** *Ec* class Ia  $\alpha_2\beta_2$  holoenzyme complex. The holoenzyme complex, shown from two different views (A and B), was generated by alignment of the R2 dimer ( $\beta_2$ ) with the R1 dimer ( $\alpha_2$ ).<sup>14</sup> Overlaid with the class Ib *Bc* NrdI-Fe<sub>2</sub>-NrdF complex. NrdI protrudes into the  $\alpha_2\beta_2$  interface, interfering with binding to the R1 dimer.

observed between NrdI from the *Bc* NrdI-NrdF crystal complex and *Bc* NrdI (PDB id: 2X2O)<sup>23</sup> (RMSD calculated to 0.37 Å) and between Fe<sub>2</sub>-NrdF and NrdF from the *Bc* NrdI-NrdF crystal complex (RMSD calculated to 0.54 Å).

**Investigation of the Possible NrdI-NrdF-NrdE Interface.** Given that NrdI is required for Mn<sup>III</sup><sub>2</sub>-Y• cofactor generation,<sup>24</sup> it is important to gain information about how NrdI-NrdF assembly effects NrdF-NrdE holoenzyme formation. A model of the  $\alpha_2\beta_2$  holoenzyme structure was first proposed by Uhlin and Eklund in 1994<sup>14</sup> for the class Ia RNR. Complementarity was shown between the  $\alpha_2$  (NrdA) dimer and the upper part of the heart-shaped structure of the  $\beta_2$  (NrdB) dimer, and a model was constructed with the 2-fold axes of the dimers superimposed. The proposed holoenzyme is believed to form a compact complex, where the binding surface of the NrdB dimer contains a region of high conservation.<sup>14</sup> A high extent of amino acid conservation in the corresponding region has also been addressed for various class Ib NrdF structures, through a sequence alignment study performed by Boal et al.<sup>33</sup> Also, high amino acid sequence conservation was shown for the NrdI-NrdF interface. The *Bc* NrdI-NrdF complex interface supports NrdI binding in the same general location on all NrdFs, as suggested previously.<sup>33</sup> In this study, we report that binding of NrdI to NrdF can disturb the  $\alpha_2\beta_2$

holocomplex formation in class Ib RNRs, contrary to what was previously suggested by Zhang et al.<sup>29</sup> The NrdI-NrdF complex assembly in *Bc* introduces steric clashes in the binding site between  $\alpha_2$  and  $\beta_2$  in the proposed holocomplex assembly, possibly preventing the suggested holoenzyme complex formation. A structural alignment of the *Bc* NrdI-NrdF structure with the *Ec*  $\alpha_2\beta_2$  holoenzyme structure, generated using the original class Ia  $\alpha_2\beta_2$  holocomplex coordinates, is shown in Figure 7. The two aligned dimeric class Ia and Ib R2 structures share a structural homology with an RMSD of 2.6 Å. These findings could possibly indicate the role of a different holocomplex interaction for the class Ib RNRs, which, contrary to the class Ia RNRs, require an additional binding partner, NrdI, for Mn<sup>III</sup><sub>2</sub>-Y• cofactor assembly. However, recent studies of *Ec* RNR support the active prokaryotic form of the enzyme with an  $\alpha_2\beta_2$  stoichiometry.<sup>15,44</sup> Conversely, another likely possibility supporting the  $\alpha_2\beta_2$  holoenzyme structure by Uhlin and Eklund is that the activation of the Mn<sup>III</sup><sub>2</sub>-Y• cofactor occurs in an initial stage prior to R1-R2 interaction in the  $\alpha_2\beta_2$  complex. This would result in NrdI dissociation prior to  $\alpha_2\beta_2$  holoenzyme formation, thereby preventing structural clashes between the respective binding partners. The structural requirement of NrdI dissociation prior to NrdE binding to NrdF could be supported by, as well as further explain, previous

activity and binding studies in *Ec*, *Bc*, and *Ba*. In *Ec*, a tight association between NrdI and NrdF has been reported,<sup>18</sup> and if NrdI needs to dissociate before NrdE can bind, this could explain the observed lower RNR specific activity of Fe-NrdF-NrdE in the presence of NrdI, resulting in an inhibitory effect, compared to a 4-fold higher specific activity in the absence of NrdI.<sup>18</sup> In contrast, in the case of *Bacillus* species, where the interaction between NrdF and NrdI has been shown to be weak,<sup>22,27</sup> NrdI does not inhibit Fe<sup>III</sup><sub>2</sub>-Y• cofactor generation (in *Ba* and *Bc*)<sup>28</sup> or RNR enzymatic activity (in *Ba*<sup>27</sup> and *Bc*<sup>28</sup>), indicating that the weaker NrdI-NrdF association in *Ba* and *Bc* makes NrdF more accessible for NrdE binding. Additionally, the removal of NrdI after activation of Mn-NrdF by NrdI does not increase specific activity in *Ba* and *Bc* or influence the binding of NrdH-thioredoxin to NrdE.<sup>27</sup> However, this type of investigation has not been reported for the *Ec* Mn-containing RNR, which might result in higher *in vitro* specific activity proceeding from NrdI removal, as a result of NrdI's tight association with NrdF. The  $\alpha_2\beta_2$  holoenzyme model by Uhlin and Eklund could then be valid also for class Ib. Whether the differences between *Ec* and *Bacillus* species could be related to the presence of the additional class Ia RNR in *Ec* should be further investigated. The conserved NrdI binding to NrdF could be of great importance in the development of antimicrobial drugs, depending on the organisms degree of NrdI-NrdF affinity. Moreover, an alteration in the NrdF interface responsible for binding of NrdI as well as NrdE could strongly affect active class Ib RNR activation and holoenzyme assembly. An overlay of *Bc* NrdI-NrdF with the *St* R1-R2 crystallographic complex from Uppsten et al.<sup>45</sup> also results in some clashes (Supplementary Figure S7A). In contrast, an overlay of the *Bc* NrdI-NrdF structure and the inactive  $\alpha_4\beta_4$  *Ec* structure<sup>46</sup> gives no structural clashes between NrdI and NrdB (Supplementary Figure S7B). Moreover, additional studies for investigation of class Ib RNR interactions and active holoenzyme formation are still required.

**Conclusion.** The *Bc* NrdI-NrdF complex structure presented in this paper strongly resembles the previously solved NrdI-NrdF complex from *Ec*,<sup>25</sup> showing only small variations in NrdI binding to NrdF in class Ib RNRs. The flexibility in key coordinating residues of the dimetal sites in *Bc* NrdI-NrdF and NrdF structures supports the suggestion that different active site geometries can serve as starting points for metallocofactor activation. However, Glu161 (*Bc* numbering) seems to be a key residue in distinguishing between the Fe and Mn activated structures. The higher tendency of Glu161 for a  $\mu$ -1,3 coordination in Mn structures, as now seen in both *Ec* and *Bc*, in contrast to the bidentate coordination seen in Fe structures, opens up for a water network through the proposed and highly conserved hydrophilic channel leading to the FMN site in NrdI. The channel and water network is blocked in the *Bc* NrdI-Fe<sub>2</sub>-NrdF and Fe<sub>2</sub>-NrdF structures through the bidentate coordination of Glu161 to metal site 2. The high degree of amino acid sequence conservation of core residues in the NrdI-NrdF interface supports similar NrdI-NrdF recognition in all class Ib RNRs, as indicated by the same general binding location in the crystal structures of NrdI-NrdF complexes in *Bc*, *Ec*,<sup>25</sup> and the modeled *Bs* NrdI-NrdF complex.<sup>33</sup> Since binding of NrdI to NrdF also occurs for Fe<sub>2</sub>-NrdF, not requiring NrdI for activation, the presence of Mn is not a requirement for NrdI binding. This is supported by the *Bc* NrdI-NrdF complex structure, crystallized with an Fe<sub>2</sub> site contrary to the *Ec* NrdI-Mn<sup>II</sup><sub>2</sub>-NrdF crystal structure, which is

the Mn<sup>II</sup><sub>2</sub>-containing active complex. Also, NrdI-NrdF binding seems to be conserved regardless of the structure of the metal coordination site, where different carboxylate conformations are observed for different crystal structures. Steric clashes introduced by NrdI in the NrdI-NrdF-NrdE formation presented in this study could indicate a requirement for NrdI to dissociate before NrdE can bind to NrdF; however, further investigation of the mechanism of class Ib active holoenzyme formation is required.

## METHODS

### Cloning, Expression, and Purification of *Bc* NrdF and NrdI.

*Bc* ATCC 14579 NrdF (BC1355) and NrdI (BC1353) were expressed and purified as described previously.<sup>23,38</sup> In brief, genes were cloned into the pET-22b plasmid (Novagen) prior to transformation into competent *Ec* BL21 (DE3) Gold cells (Stratagene). Cells containing the pET-22b-NrdF or -NrdI were grown in Terrific Broth medium containing 100 µg/mL ampicillin. Protein expression was induced by adding isopropyl  $\beta$ -D-1-thiogalactopyranoside to a final concentration of 0.8 mM, and the culture was incubated for 12–16 h at 20 °C with vigorous shaking before harvesting. The frozen cell paste was lysed using an X-press,<sup>47</sup> dissolved in 100 mM Tris-HCl, pH 7.5, 10 mM EDTA, and cleared from nucleic acids by streptomycin sulfate (2.5%) precipitation. Proteins were precipitated with 60% ammonium sulfate (0.43 mg/mL), dissolved in 50 mM Tris-HCl, pH 7.5, and desalted using a HiTrap Desalting column (GE Healthcare). Desalted protein was applied to a HiTrap HP Q column (GE Healthcare), and the proteins were separated with a 0–0.5 M KCl gradient. As a final polishing step, the proteins were purified on a Superdex 200 column (GE Healthcare).

**Crystallization.** All initial crystallization screening was performed with an Orxy6 crystallization robot (Douglas Instruments Ltd.).

**Crystallization of the *Bc* NrdI-NrdF Complex.** For the NrdI-NrdF complex, NrdF (monomer) and NrdI (both in 50 mM Tris-HCl, pH 7.5) were mixed in an equimolar amount. Bright yellow crystals (20 mg/mL total protein) were obtained using the sitting drop vapor diffusion method at RT with 10% (w/v) PEG 8000, 0.2 M magnesium chloride, and 0.1 M Tris, pH 7.0 (JCSG-plus Screen, Molecular Dimensions Ltd.). Crystals were briefly soaked in cryoprotectant solution (25% glycerol, 10% (w/v) PEG 8000, 0.2 M magnesium chloride, and 0.1 M Tris, pH 7.0) and flash frozen in liquid nitrogen (NrdI-NrdF-1). Yellow crystals (5 mg/mL total protein) were also obtained using the same method with 2 M sodium chloride and 0.1 M sodium citrate, pH 6.0 (ProPlex Screen, Molecular Dimensions Ltd.), soaked in cryoprotectant solution (25% PEG 400, 2 M sodium chloride, and 0.1 M sodium citrate, pH 6.0) and flash frozen in liquid nitrogen (NrdI-NrdF-2). The NrdI-NrdF crystals were not soaked in metal solutions before collecting X-ray data; however, the medium used for expression of the genes naturally contains traces of iron.

**Crystallization of *Bc* NrdFs.** Fe<sub>2</sub>-NrdF and Mn<sup>II</sup><sub>2</sub>-NrdF crystals (8 mg/mL monomer) were obtained with 0.2 M Mg-formate, 20% (w/v) PEG 3350, and 0.1 M HEPES, pH 7.5 (optimized from the JCSG-plus Screen, Molecular Dimensions Ltd.) and soaked for 20 min in cryoprotectant solution containing the mother liquor mixed with 25% PEG 400 and Fe(NH<sub>4</sub>)<sub>2</sub>(SO<sub>4</sub>)<sub>2</sub>/sulfuric acid or MnCl<sub>2</sub>, respectively. Also, two apo-NrdF structures have been solved from crystals obtained with 0.04 M H<sub>3</sub>PO<sub>4</sub>, 16% PEG 8000, and 20% glycerol (apo-NrdF-1), and with 0.2 M Mg-formate pH 5.9 and 20% PEG 3350 (apo-NrdF-2) (JCSG-plus Screen, Molecular Dimensions Ltd.), both soaked in cryoprotectant solution containing the mother liquor including 30% glycerol. Finally, all NrdF crystals were flash frozen in liquid nitrogen.

**Data Collection and Refinement.** Crystallographic data sets were collected at beamlines ID29 and ID14-1 at the European Synchrotron Radiation Facility (ESRF), Grenoble, France and at PXII-X10SA at the Swiss Light Source (SLS) at Paul Scherrer Institut, Villigen, Switzerland. The crystallographic data for NrdI-NrdF-1, as well as Fe<sub>2</sub>-NrdF and Mn<sup>II</sup><sub>2</sub>-NrdF, were collected at ID29 (ESRF), the apo-NrdF-1 and apo-NrdF-2 at ID14-1 (ESRF), and the NrdI-NrdF-2

at X10SA (SLS). Data sets were processed with MOSFLM<sup>48</sup> and scaled and merged using SCALA or AIMLESS,<sup>49,50</sup> and the space group was confirmed with POINTLESS through the CCP4 software suite.<sup>51</sup> The structures were solved by molecular replacement using PHASER.<sup>52</sup> A homologue model of *Bc* apo-NrdF modeled with SWISS-MODEL<sup>53,54</sup> from the *Ca* apo-R2 structure (PDB id: 3DHZ)<sup>42</sup> was used as a search model in PHASER to solve the *Bc* apo-NrdF-1 structure. The *Bc* apo-NrdF-1 was then used as a search model to solve the structure of apo-NrdF-2, Fe<sub>2</sub>-NrdF, and Mn<sup>II</sup><sub>2</sub>-NrdF. The NrdI-NrdF-1 structure was solved with the coordinates of *Bc* apo-NrdF-1 and *Bc* NrdI (PDB id: 2X2O) as the starting models. Refinement for all structures was done using restrained refinement in REFMAC,<sup>55</sup> and model building was performed with COOT<sup>56</sup> in multiple cycles. For the *Bc* NrdF structures, medium NCS restraints were introduced. For some of the structures, full occupancy of the metal sites gave negative density in the difference maps, and for these structures the metal content was reduced. NrdI-NrdF-1 has been refined with 90% Fe, NrdI-NrdF-2 with 50% Fe, Mn<sup>II</sup><sub>2</sub>-NrdF with one site 90% while the remaining 100% Mn, and Fe<sub>2</sub>-NrdF with 100% Fe with high B-factors. For the apo structures, one of the metal sites 1 in apo-NrdF-1 and two metal sites 1 in apo-NrdF-2 have been modeled with 25% occupancy of Fe. The absorbed X-ray doses of the different crystals during crystallographic data collection have been calculated with the program RADDOSE.<sup>57,58</sup> All structure figures were prepared using PyMOL.<sup>59</sup> All backbone root-mean-square deviation (RMSD) values were calculated using PDBeFold (<http://www.ebi.ac.uk>). The final data collection and refinement statistics are listed in Table 1 and Supplementary Table S1. The hydrophilic complex channel lining the *Bc* NrdI-NrdF interface was calculated with HOLLOW<sup>60</sup> using a 1.4 Å probe radius. As a comparison, a corresponding channel was also calculated for the *Ec* NrdI-NrdF structure.<sup>25</sup>

**Single-Crystal Light Absorption Spectroscopy.** Light absorption spectroscopy was carried out on single crystals (frozen as described above) of *Bc* NrdI and *Bc* NrdI-NrdF. The experiments were performed at beamline X10SA and SLSpectroLAB at SLS. Spectra were recorded with an on-axis built microspectrophotometer system with an Andor 303i Czerny–Turner spectrograph and a Newton electron multiplying CCD (Andor Technology).<sup>61</sup>

## ■ ASSOCIATED CONTENT

### Supporting Information

Supplementary table and figures. This material is available free of charge via the Internet at <http://pubs.acs.org>.

### Accession Codes

The coordinates and structure factors (codes 4BMO, 4BMP, 4BMQ, 4BMR, 4BMT, and 4BMU) have been deposited in the Protein Data Bank through EMBL-EBI (<http://www.pdbe.org>) and are listed in Table 1 and Supplementary Table S1.

## ■ AUTHOR INFORMATION

### Corresponding Author

\*E-mail: h.p.hersleth@ibv.uio.no.

### Notes

The authors declare no competing financial interest.

## ■ ACKNOWLEDGMENTS

We thank B. Dalhus for access to crystallization screening at the Regional Core Facility for Structural Biology and Bioinformatics at the South-Eastern Norway Regional Health Authority (Grants no. 2009100 and 2011040). We gratefully acknowledge the Swiss-Light-Source SLS (20111245) for providing beam time with online microspectrophotometry and help from the team at X10SA and G. Pompidor for assistance with the on-axis online microspectrophotometer. We gratefully acknowledge the European Synchrotron Radiation Facility ESRF (MX10156) for providing beam time, and the team at ID29 and ID14-1 for

their assistance. The coordinates for the *E. coli* class Ia  $\alpha_2\beta_2$  holoenzyme structure were kindly provided by U. Uhlin, Uppsala University, Uppsala, Sweden. We acknowledge financial support from the Norwegian Research Council through projects 214239/F20 and 218412/F50 (K.K.A.), MLS<sup>UIO</sup> program for Molecular Life Science research at the University of Oslo through the PX-Oslo X-ray core facilities and the Norwegian Cancer Society 539012 (K.K.A.) and CMST COST Action CM1003 and financial support for synchrotron travel from the Norwegian Research Council through projects 138370/V30 and 216625/F50 (K.K.A.) and from the European Community's Seventh Framework Programme (FP7/2007-2013) under BioStruct-X (grant agreement No. 283570) on project 1760 (K.K.A./H.P.H.).

## ■ ABBREVIATIONS

RNR, ribonucleotide reductase; *Bc*, *Bacillus cereus*; *Ec*, *Escherichia coli*; *Mt*, *Mycobacterium tuberculosis*; *Ca*, *Corynebacterium ammoniagenes*; *Ba*, *Bacillus anthracis*; *St*, *Salmonella typhimurium*; FMN, flavin mononucleotide cofactor; ESRF, European Synchrotron Research Facility; SLS, Swiss-Light-Source; RMSD, root-mean-square deviation

## ■ REFERENCES

- (1) Nordlund, N., and Reichard, P. (2006) Ribonucleotide reductases. *Annu. Rev. Biochem.* **75**, 681–706.
- (2) Tomter, A. B., Zoppellaro, G., Andersen, N. H., Hersleth, H. P., Hammerstad, M., Rohr, A. K., Sandvik, G. K., Strand, K. R., Nilsson, G. E., Bell, C. B., Barra, A. L., Blasco, E., Le Pape, L., Solomon, E. I., and Andersson, K. K. (2013) Ribonucleotide reductase class I with different radical generating clusters. *Coord. Chem. Rev.* **257**, 3–26.
- (3) Andersson, K. K., Ed. (2008) *Ribonucleotide Reductase*, Nova Science Publishers, Inc., Hauppauge, NY.
- (4) Cotruvo, J. A., and Stubbe, J. (2011) Class I ribonucleotide reductases: Metallocofactor assembly and repair in vitro and in vivo. *Annu. Rev. Biochem.* **80**, 733–767.
- (5) Tomter, A. B., Zoppellaro, G., Schmitzberger, F., Andersen, N. H., Barra, A. L., Engman, H., Nordlund, P., and Andersson, K. K. (2011) HF-EPR, Raman, UV/VIS light spectroscopic, and DFT studies of the ribonucleotide reductase R2 tyrosyl radical from Epstein-Barr virus. *PLoS One* **6**, e25022.
- (6) Kolberg, M., Strand, K. R., Graff, P., and Andersson, K. K. (2004) Structure, function, and mechanism of ribonucleotide reductases. *Biochim. Biophys. Acta, Proteins Proteomics* **1699**, 1–34.
- (7) Atkin, C. L., Thelander, L., Reichard, P., and Lang, G. (1973) Iron and free-radical in ribonucleotide reductase - exchange of iron and mossbauer-spectroscopy of protein-b2 subunit of *Escherichia coli* enzyme. *J. Biol. Chem.* **248**, 7464–7472.
- (8) Jiang, W., Yun, D., Saleh, L., Barr, E. W., Xing, G., Hoffart, L. M., Maslak, M. A., Krebs, C., and Bollinger, J. M. (2007) A manganese(IV)/iron(III) cofactor in *Chlamydia trachomatis* ribonucleotide reductase. *Science* **316**, 1188–1191.
- (9) Hogbom, M., Stenmark, P., Voevodskaya, N., McClarty, G., Graslund, A., and Nordlund, P. (2004) The radical site in chlamydial ribonucleotide reductase defines a new R2 subclass. *Science* **305**, 245–248.
- (10) Roshick, C., Iliffe-Lee, E. R., and McClarty, G. (2000) Cloning and characterization of ribonucleotide reductase from *Chlamydia trachomatis*. *J. Biol. Chem.* **275**, 38111–38119.
- (11) Voevodskaya, N., Lendzian, F., Ehrenberg, A., and Graslund, A. (2007) High catalytic activity achieved with a mixed manganese-iron site in protein R2 of *Chlamydia* ribonucleotide reductase. *FEBS Lett.* **581**, 3351–3355.
- (12) Lundin, D., Torrents, E., Poole, A. M., and Sjoberg, B. M. (2009) RNRdb, a curated database of the universal enzyme family

- ribonucleotide reductase, reveals a high level of misannotation in sequences deposited to Genbank. *BMC Genomics* 10, 589.
- (13) Eriksson, M., Jordan, A., and Eklund, H. (1998) Structure of *Salmonella typhimurium* nrdF ribonucleotide reductase in its oxidized and reduced forms. *Biochemistry* 37, 13359–13369.
- (14) Uhlin, U., and Eklund, H. (1994) Structure of ribonucleotide reductase protein R1. *Nature* 370, 533–539.
- (15) Logan, D. T. (2011) Closing the circle on ribonucleotide reductases. *Nat. Struct. Mol. Biol.* 18, 251–253.
- (16) Jordan, A., Pontis, E., Atta, M., Krook, M., Gibert, I., Barbe, J., and Reichard, P. (1994) A 2nd class-I ribonucleotide reductase in enterobacteriaceae - characterization of the *Salmonella-typhimurium* enzyme. *Proc. Natl. Acad. Sci. U.S.A.* 91, 12892–12896.
- (17) Huque, Y., Fieschi, F., Torrents, E., Gibert, I., Eliasson, R., Reichard, P., Sahlin, M., and Sjöberg, B. M. (2000) The active form of the R2F protein of class Ib ribonucleotide reductase from *Corynebacterium ammoniagenes* is a diferric protein. *J. Biol. Chem.* 275, 25365–25371.
- (18) Cotruvo, J. A., and Stubbe, J. (2010) An active dimanganese-(III)-tyrosyl radical cofactor in *Escherichia coli* class Ib ribonucleotide reductase. *Biochemistry* 49, 1297–1309.
- (19) Cox, N., Ogata, H., Stolle, P., Reijerse, E., Auling, G., and Lubitz, W. (2010) A tyrosyl-dimanganese coupled spin system is the native metalloradical cofactor of the R2F subunit of the ribonucleotide reductase of *Corynebacterium ammoniagenes*. *J. Am. Chem. Soc.* 132, 11197–11213.
- (20) Tomter, A. B., Zoppellaro, G., Bell, C. B., Barra, A. L., Andersen, N. H., Solomon, E. I., and Andersson, K. K. (2012) Spectroscopic studies of the iron and manganese reconstituted tyrosyl radical in *Bacillus cereus* ribonucleotide reductase R2 protein. *PLoS One* 7, e33436.
- (21) Cotruvo, J. A., and Stubbe, J. (2008) NrdI, a flavodoxin involved in maintenance of the diferric-tyrosyl radical cofactor in *Escherichia coli* class Ib ribonucleotide reductase. *Proc. Natl. Acad. Sci. U.S.A.* 105, 14383–14388.
- (22) Johansson, R., Torrents, E., Lundin, D., Sprenger, J., Sahlin, M., Sjöberg, B. M., and Logan, D. T. (2010) High-resolution crystal structures of the flavoprotein NrdI in oxidized and reduced states - an unusual flavodoxin. *FEBS J.* 277, 4265–4277.
- (23) Rohr, A. K., Hersleth, H. P., and Andersson, K. K. (2010) Tracking flavin conformations in protein crystal structures with Raman spectroscopy and QM/MM calculations. *Angew. Chem., Int. Ed.* 49, 2324–2327.
- (24) Cotruvo, J. A., and Stubbe, J. (2011) *Escherichia coli* class Ib ribonucleotide reductase contains a dimanganese(III)-tyrosyl radical cofactor in vivo. *Biochemistry* 50, 1672–1681.
- (25) Boal, A. K., Cotruvo, J. A., Stubbe, J., and Rosenzweig, A. C. (2010) Structural basis for activation of class Ib ribonucleotide reductase. *Science* 329, 1526–1530.
- (26) Cotruvo, J. A., Stich, T. A., Britt, D. R., and Stubbe, J. (2013) Mechanism of assembly of the dimanganese-tyrosyl radical cofactor of class Ib ribonucleotide reductase: Enzymatic generation of superoxide is required for tyrosine oxidation via a Mn(III)Mn(IV) intermediate. *J. Am. Chem. Soc.* 135, 4027–4039.
- (27) Crona, M., Torrents, E., Rohr, A. K., Hofer, A., Furrer, E., Tomter, A. B., Andersson, K. K., Sahlin, M., and Sjöberg, B. M. (2011) NrdH-Redoxin protein mediates high enzyme activity in manganese-reconstituted ribonucleotide reductase from *Bacillus anthracis*. *J. Biol. Chem.* 286, 33053–33060.
- (28) Tomter, A. B. (2010) Spectroscopic Studies of the Ribonucleotide Reductase R2-subunit from Mammals, Virus, and Bacteria, In *Faculty of Mathematics and Natural Sciences*, University of Oslo, Oslo, Norway.
- (29) Zhang, Y., and Stubbe, J. (2011) *Bacillus subtilis* class Ib ribonucleotide reductase is a dimanganese(III)-tyrosyl radical enzyme. *Biochemistry* 50, 5615–5623.
- (30) Hogbom, M., Huque, Y., Sjöberg, B. M., and Nordlund, P. (2002) Crystal structure of the di-iron/radical protein of ribonucleotide reductase from *Corynebacterium ammoniagenes*. *Biochemistry* 41, 1381–1389.
- (31) Solomon, E. I., Brunold, T. C., Davis, M. I., Kemsley, J. N., Lee, S. K., Lehnert, N., Neese, F., Skulan, A. J., Yang, Y. S., and Zhou, J. (2000) Geometric and electronic structure/function correlations in non-heme iron enzymes. *Chem. Rev.* 100, 235–349.
- (32) Uppsten, M., Davis, J., Rubin, H., and Uhlin, U. (2004) Crystal structure of the biologically active form of class 1b ribonucleotide reductase small subunit from *Mycobacterium tuberculosis*. *FEBS Lett.* 569, 117–122.
- (33) Boal, A. K., Cotruvo, J. A., Stubbe, J., and Rosenzweig, A. C. (2012) The dimanganese(II) site of *Bacillus subtilis* class Ib ribonucleotide reductase. *Biochemistry* 51, 3861–3871.
- (34) Henderson, R. (1990) Cryoprotection of protein crystals against radiation-damage in electron and x-ray-diffraction. *Proc. R. Soc. London, Ser. B* 241, 6–8.
- (35) Hersleth, H.-P., and Andersson, K. K. (2011) How different oxidation states of crystalline myoglobin are influenced by X-rays. *Biochim. Biophys. Acta, Proteins Proteomics* 1814, 785–796.
- (36) Griese, J. J., and Hogbom, M. (2012) X-ray reduction correlates with soaking accessibility as judged from four non-crystallographically related diiron sites. *Metallomics* 4, 894–898.
- (37) Sigfridsson, K. G. V., Chernev, P., Leidel, N., Popovic-Bijelic, A., Graslund, A., and Haumann, M. (2013) Rapid X-ray photoreduction of dimetal-oxygen cofactors in ribonucleotide reductase. *J. Biol. Chem.* 288, 9648–9661.
- (38) Tomter, A. B., Bell, C. B., Rohr, A. K., Andersson, K. K., and Solomon, E. I. (2008) Circular dichroism and magnetic circular dichroism studies of the biferrous site of the class Ib ribonucleotide reductase from *Bacillus cereus*: Comparison to the class Ia enzymes. *Biochemistry* 47, 11300–11309.
- (39) Strand, K. R., Karlsen, S., Kolberg, M., Rohr, A. K., Gorbitz, C. H., and Andersson, K. K. (2004) Crystal structural studies of changes in the native dinuclear iron center of ribonucleotide reductase protein R2 from mouse. *J. Biol. Chem.* 279, 46794–46801.
- (40) Ubbink, M. (2012) Dynamics in transient complexes of redox proteins. *Biochem. Soc. Trans.* 40, 415–418.
- (41) Nordlund, P., and Eklund, H. (1993) Structure and function of the *Escherichia coli* ribonucleotide reductase protein R2. *J. Mol. Biol.* 232, 123–164.
- (42) Smith, P., Zhou, B. S., Ho, N., Yuan, Y. C., Su, L., Tsai, S. C., and Yen, Y. (2009) 2.6 Ångstrom X-ray crystal structure of human p53R2, a p53-inducible ribonucleotide reductase. *Biochemistry* 48, 11134–11141.
- (43) Wilmot, C. M., Sjögren, T., Carlsson, G. H., Berglund, G. I., and Hajdu, J. (2002) Defining redox state of X-ray crystal structures by single-crystal ultraviolet-visible microspectrophotometry. *Methods Enzymol.* 353, 301–318.
- (44) Rofougaran, R., Crona, M., Vodnala, M., Sjöberg, B. M., and Hofer, A. (2008) Oligomerization status directs overall activity regulation of the *Escherichia coli* class Ia ribonucleotide reductase. *J. Biol. Chem.* 283, 35310–35318.
- (45) Uppsten, M., Farnegardh, M., Domkin, V., and Uhlin, U. (2006) The first holocomplex structure of ribonucleotide reductase gives new insight into its mechanism of action. *J. Mol. Biol.* 359, 365–377.
- (46) Ando, N., Brignole, E. J., Zimanyi, C. M., Funk, M. A., Yokoyama, K., Asturias, F. J., Stubbe, J., and Drennan, C. L. (2011) Structural interconversions modulate activity of *Escherichia coli* ribonucleotide reductase. *Proc. Natl. Acad. Sci. U.S.A.* 108, 21046–21051.
- (47) Magnusson, K. E., and Edebo, L. (1976) Influence of cell concentration, temperature, and press performance on flow characteristics and disintegration in freeze-pressing of *Saccharomyces cerevisiae* with X-press. *Biotechnol. Bioeng.* 18, 865–883.
- (48) Powell, H. R. (1999) The Rossmann Fourier autoindexing algorithm in MOSFLM. *Acta Crystallogr., Sect. D: Biol. Crystallogr.* 55, 1690–1695.
- (49) Evans, P. (2006) Scaling and assessment of data quality. *Acta Crystallogr., Sect. D: Biol. Crystallogr.* 62, 72–82.

- (50) Evans, P. R. (2011) An introduction to data reduction: space-group determination, scaling and intensity statistics. *Acta Crystallogr., Sect. D: Biol. Crystallogr.* 67, 282–292.
- (51) Winn, M. D., Ballard, C. C., Cowtan, K. D., Dodson, E. J., Emsley, P., Evans, P. R., Keegan, R. M., Krissinel, E. B., Leslie, A. G. W., McCoy, A., McNicholas, S. J., Murshudov, G. N., Pannu, N. S., Potterton, E. A., Powell, H. R., Read, R. J., Vagin, A., and Wilson, K. S. (2011) Overview of the CCP4 suite and current developments. *Acta Crystallogr., Sect. D: Biol. Crystallogr.* 67, 235–242.
- (52) McCoy, A. J., Grosse-Kunstleve, R. W., Storoni, L. C., and Read, R. J. (2005) Likelihood-enhanced fast translation functions. *Acta Crystallogr., Sect. D: Biol. Crystallogr.* 61, 458–464.
- (53) Arnold, K., Bordoli, L., Kopp, J., and Schwede, T. (2006) The SWISS-MODEL workspace: a web-based environment for protein structure homology modelling. *Bioinformatics* 22, 195–201.
- (54) Kiefer, F., Arnold, K., Kunzli, M., Bordoli, L., and Schwede, T. (2009) The SWISS-MODEL Repository and associated resources. *Nucleic Acids Res.* 37, D387–D392.
- (55) Murshudov, G. N., Vagin, A. A., and Dodson, E. J. (1997) Refinement of macromolecular structures by the maximum-likelihood method. *Acta Crystallogr., Sect. D: Biol. Crystallogr.* 53, 240–255.
- (56) Emsley, P., and Cowtan, K. (2004) Coot: model-building tools for molecular graphics. *Acta Crystallogr., Sect. D: Biol. Crystallogr.* 60, 2126–2132.
- (57) Murray, J. W., Garman, E. F., and Ravelli, R. B. G. (2004) X-ray absorption by macromolecular crystals: the effects of wavelength and crystal composition on absorbed dose. *J. Appl. Crystallogr.* 37, 513–522.
- (58) Paithankar, K. S., Owen, R. L., and Garman, E. F. (2009) Absorbed dose calculations for macromolecular crystals: improvements to RADDOSE. *J. Synchrotron Radiat.* 16, 152–162.
- (59) Delano, W. L. (2002) *The PyMOL Molecular Graphics System*, DeLano Scientific, San Carlos, CA.
- (60) Ho, B. K., and Gruswitz, F. (2008) HOLLOW: Generating accurate representations of channel and interior surfaces in molecular structures. *BMC Struct. Biol.* 8, 49.
- (61) Owen, R. L., Pearson, A. R., Meents, A., Boehler, P., Thominet, V., and Schulze-Briese, C. (2009) A new on-axis multimode spectrometer for the macromolecular crystallography beamlines of the Swiss Light Source. *J. Synchrotron Radiat.* 16, 173–182.